Metals & corrosion

Effect of high-temperature supercritical carbon dioxide exposure on the microstructure and tensile properties of diffusion-bonded Alloy 690

Hongsheng Chen[1,2], Sung Hwan Kim[1], and Changheui Jang[1,*]

[1] *Department of Nuclear and Quantum Engineering, Korea Advanced Institute of Science and Technology, Daejeon 34141, Republic of Korea*
[2] *Shenzhen Clean Energy Research Institute, Shenzhen 518000, People's Republic of China*

ABSTRACT

Alloy 690 was diffusion-bonded and exposed to the high-temperature super-critical CO_2 environment, and the effect of exposure on the microstructure and mechanical properties was investigated. In the as-bonded joint, some small carbides are discontinuously arranged along the bonding line. After exposure at 550 °C and 600 °C, the continuous carbides are developed and occupy all the grain boundaries and bonding line. The continuous carbides transform into the discrete large particles when the exposure temperature further increases to 650 °C. With the increase in exposure temperature, the tensile strength and microhardness of the joints decrease, while the elongation first slightly increases and then decreases at 650 °C. For the as-bonded joint and the joints exposed at 550 °C and 600 °C, the fracture occurs at the parent Alloy 690 and the main fracture mode is the ductile dimple fracture. However, for the joint exposed at 650 °C, the fracture occurs at the bond line with a manner of brittle fracture. The degradation of strengths and elongation after exposure to supercritical CO_2 at 650 °C were associated with the growth of carbides along the bond line.

Introduction

The Brayton cycle with supercritical carbon dioxide (S-CO_2) is under consideration for an alternative power conversion cycle to substitute the conventional steam Rankine cycle, because this power cycle can obtain higher thermal efficiencies near 50% by taking advantage of fluid properties of S-CO_2 [1]. S-CO_2 power cycle can be used in many applications, such as Gen IV nuclear reactors, fossil fuel power plants, waste heat recovery, concentrated solar power, geothermal and biofuel plants [1–4]. In the systems of S-CO_2 power cycle, heat exchangers are critical components and the effectiveness of heat exchangers is directly associated with the overall efficiency of plants [5]. Correspondingly, compact heat exchangers with higher effectiveness are typically identified

for S-CO$_2$ power cycle, which usually bear the high thermal duty and need to operate at high temperature and high pressure [1, 6]. At present, the printed circuit heat exchanger (PCHE), one of the compact heat exchangers, is widely chosen as the heat exchanger for the nuclear application because of its superior effectiveness, robustness and compactness [5]. The PCHEs are usually constructed by the diffusion bonding of multiple etched plates with many micro-channels. To maintain the entire system integrity, the diffusion-bonded joints of PCHEs must be sufficiently robust during the operation process of S-CO$_2$ power cycle [7].

Ni-based alloys are often used for constructing the PCHEs because these alloys possess higher corrosion resistance and superior mechanical strengths at high temperatures [8]. Many studies have been conducted to evaluate the corrosion behaviors of many candidate Ni-based alloys in the high-temperature S-CO$_2$ environment [9–15]. Compared with traditional ferritic–martensitic and austenitic steels [16–20], Ni-based alloys exhibited the best corrosion resistance, because a protective chromia (Cr$_2$O$_3$) layer could be developed on the Ni-based alloys [13, 14], while less protective scales with outer magnetite (Fe$_3$O$_4$) and inner spinel oxides ((Fe, Cr, Mn)$_3$O$_4$) were usually formed on the ferritic–martensitic and austenitic steels [19, 20]. Moreover, the corrosion resistance of alloys could be distinctly improved by Al alloying in the matrix or by deposition of Al-rich layers on the alloy surface to form α-Al$_2$O$_3$ layer [21–24]. The α-Al$_2$O$_3$ layer exhibited superior corrosion and carburization resistance in the high-temperature S-CO$_2$ environment, and the amorphous carbon layer, which was usually formed at the oxide/matrix interface of the conventional Ni-based alloys, could be suppressed in the Ni-based alloys with α-Al$_2$O$_3$ film [22].

On the other hand, the diffusion bonding of Ni-based alloys for the PCHE application was conducted by many researchers [8, 25–31]. As early as the end of the last century, Takeda et al. [25] proposed a small-scale concavo-convex plate-type compact heat exchanger for the next-generation reactors. These concavo-convex plates were made of Ni-based superalloy (Hastelloy XR) and were successfully welded by diffusion bonding at 1100 °C and 1150 °C, verifying the feasibility of diffusion bonding method for fabricating the compact heat exchanger [25]. After that, a lot of studies were carried out to optimize the

diffusion bonding parameters of Ni-based alloys and the structural parameters of the PCHE [26–30]. The bonding temperatures, bonding durations, compression stresses and roughness of bonding surface and other parameters had an impact on the microstructure and mechanical properties of diffusion-bonded Ni-based alloys [28].

However, there are rarely published reports on the performance of diffusion-bonded Ni-based alloys in the high-temperature S-CO$_2$ environment. Recently, the present authors investigated the behaviors of the diffusion-bonded joints of Alloy 600 in the S-CO$_2$ environment at 550 °C and 650 °C and found that the oxidation characteristics at the diffusion-bonded regions were similar to the parent Ni-based alloys [12]. However, the influence of exposure in S-CO$_2$ environment on the mechanical properties of the diffusion-bonded joints was not included in this work. For the PCHE application, the diffusion-bonded joints should be robust enough to maintain the integrity, as mentioned previously. The mechanical properties of the diffusion-bonded joints are very important factors to evaluate the fabricated and served PCHE.

Based on the above considerations, the present work aims to investigate the microstructures of the bonding regions and the mechanical properties of the diffusion-bonded joints before and after exposure in the S-CO$_2$ environment. The exposure conditions are chosen to be 550 °C, 600 °C and 650 °C, respectively, with a fixed pressure of 20 MPa for the potential application to next-generation nuclear systems [32]. The effect of exposure temperature on the microstructures and mechanical properties of the joints will be emphatically assessed in the present study.

Experimental procedures

Materials and diffusion bonding

Alloy 690 was chosen for the diffusion-bonded joints in the present study. This alloy is widely used for steam generator tubes, hardware, baffles and tube-sheets in the nuclear power plants, which has excellent resistance to many high-temperature corrosive media. Previous studies also verify the superior corrosion and carburization resistance of Alloy 690 in the high-temperature S-CO$_2$ environments [10, 11].

The chemical composition of the as-received Alloy 690 was analyzed by the inductively coupled plasma spectroscopy, and the results are shown in Table 1.

The as-received Alloy 690 was machined into blocks with a dimension of 25 mm × 20 mm × 12 mm. Prior to diffusion bonding, the bonding surfaces were mechanically ground and polished with silicon carbide papers (up to 1200 grit) and then were ultrasonically cleaned by ethanol. Diffusion bonding of the Alloy 690 blocks was carried out by a local contractor, TNP Corporation. The schematic diagram of the diffusion-bonded block is shown in Fig. 1a. For Alloy 690, a bonding temperature of 1070 °C, bonding duration of 1 h and compressive stress of 9 MPa were used. These bonding parameters were selected based on our preliminary studies. The bonding temperature was set near the solution temperature of carbides in Alloy 690, the bonding stress was set to not cause obvious deformation of the blocks during diffusion bonding, and the bonding duration was limited to 1 h to avoid excessive grain growth. In order to recover the ductility of the bonded joints, these bonded Alloy 690 blocks were subjected to post-bond heat treatments after diffusion bonding [31]. The post-bond heat treatments were conducted at 1010 °C for 20 h in a vacuum furnace with a vacuum less than 10^{-3} Pa.

Exposure to high-temperature S-CO$_2$ environment

After diffusion bonding and post-bond heat treatments, diffusion-bonded Alloy 690 blocks were electric discharge machined into mini-sized tensile specimens while keeping the diffusion bonding line at the center of the specimen. The dimension of mini-sized tensile specimens is shown in Fig. 1b. For hanging the mini-sized specimens during the corrosion testing, a small hole of 1.5 mm in diameter was drilled in one of two heads of the specimens.

Corrosion tests of these diffusion-bonded specimens were conducted in a high-temperature S-CO$_2$ corrosion testing facility. The details of the S-CO$_2$ corrosion testing facility were described in a previous publication by the authors [10]. These diffusion-bonded specimens were hung on a platinum wire of 0.5 mm in diameter and were separated from each other by alumina spacers. Then, the hung specimens were fixed in an alumina boat and loaded into the autoclave of the S-CO$_2$ corrosion testing facility. At least three diffusion-bonded specimens were used for each condition. Prior to heating, the research-grade CO$_2$ gas (99.999% purity) was fed into the corrosion system to remove the residual air for 5 min. Then, CO$_2$ was pressurized into the corrosion system by a high-pressure supercritical pump (Scientific Systems Incorporation). The pressurized CO$_2$ was firstly heated to 400 °C by a helical-type preheater and then pressurized onto the testing autoclave to be fully heated to the target temperatures. Isothermal corrosion tests were carried out at 550 °C, 600 °C and 650 °C for 1000 h. During the corrosion testing, the pressure of S-CO$_2$ was fixed at 20 MPa by using a back pressure regulator and the flow rate of S-CO$_2$ was maintained at 5 ml/min.

Characterization of the diffusion-bonded joints

Considering the fact that the diffusion-bonded surface regions are very small compared with the entire specimens, the weight gains of diffusion-bonded specimens should be the same as the conventional specimens. Many weight gain results of conventional Alloy 690 in the S-CO$_2$ environment have been achieved in previous studies [10, 11]; thus, the weighing tests are not included in the present study. After removing the specimens from the test autoclave, the tensile tests were conducted at room temperature to evaluate the strengths of the diffusion-bonded specimens by using a small tensile testing machine (Instron 4204) with a constant strain rate of 3.33×10^{-4} s^{-1}. Two specimens were tested to check the repeatability for each condition.

The microstructures of the as-received Alloy 690 and diffusion-bonded joint before corrosion test were examined by a scanning electron microscope (SEM, Magellan 400) equipped with an electron backscatter diffraction (EBSD, EDAX Hikari). The surface and cross-sectional microstructures and chemical compositions of the diffusion-bonded joints before and after S-CO$_2$ exposure (or, corrosion test) were characterized by SEM equipped with an energy-

Table 1 Chemical compositions (in wt%) of Alloy 690 in the present study

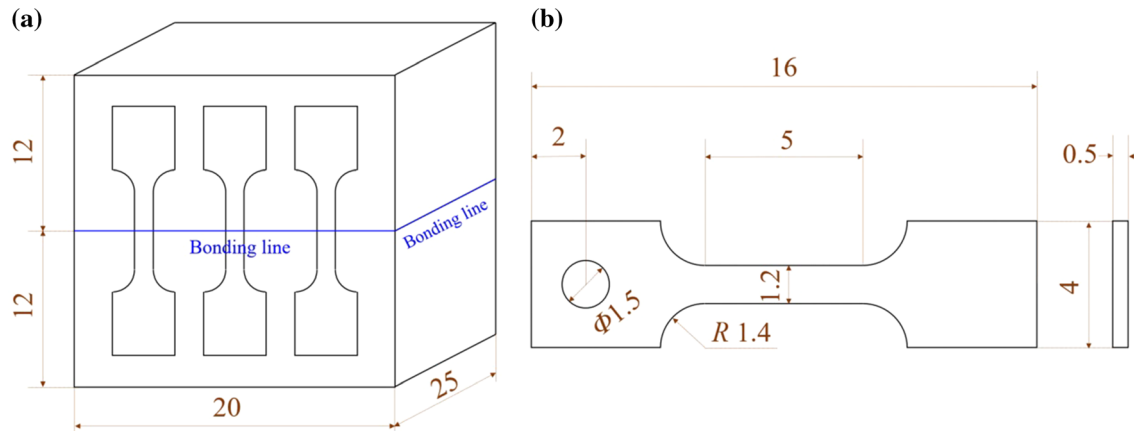| Materials	Ni	Cr	Fe	Mn	Ti	Al	Si	C	Cu
Alloy 690	Bal.	28.4	8.3	0.2	0.26	0.3	0.2	0.02	0.01

(a)

(b)

Figure 1 Schematic diagram of **a** the diffusion-bonded blocks and **b** the mini-sized tensile specimens (dimension in mm).

dispersive X-ray spectroscope (EDS, EDAX). The fracture morphologies were also examined by SEM and EDS after the tensile test. To determine the grain size of the as-received Alloy 690 and the diffusion-bonded Alloy 690, a line-intercept method was used to measure the average grain size based on the EBSD and SEM images. In order to obtain more accurate grain size, at least five different images and one hundred grains were measured for each condition. Finally, the Vickers microhardnesses of the joints were measured on the polished cross-sectional surfaces by a hardness tester (Wolpert Wilson Instruments) exerting a 200 g load with a duration of 10 s; it should be noted that the microhardness was measured on the crystal grains near the bond line (not including grain boundaries) to exclude the effect of carbides. At least 10 microhardness tests were conducted for each condition.

Results and discussion

Microstructure of the diffusion-bonded joint

Figure 2a shows the typical EBSD microstructure of the as-received Alloy 690 with an average grain size of ∼ 100 μm. Also, there are many annealing twins with band morphologies in the grains. After diffusion bonding and post-bond heat treatments, a fine structure with a smaller average grain size of ∼ 60 μm is achieved in the diffusion-bonded joint, as shown in Fig. 2b. Considering that the Alloy 690 diffusion-bonded joints are subjected to plastic deformation due to the compressive bonding stress,

dynamic and/or static recrystallization may have occurred during the diffusion bonding process [33]. In addition, it can be clearly seen from the high-magnification images that the size of grains adjacent to the bond line is smaller than that far from the bond line, as shown in Fig. 2c, d. This suggests that the plastic strain at the bonding region is somewhat larger than the remaining regions. Meanwhile, it is well known that the recrystallized grain size has a strong correlation with the plastic strains, and finer grains can be achieved by increasing the effective strain [34]. Consequently, smaller grains were achieved at the bonding regions of the joint after the high-temperature diffusion bonding.

It should be noted that the bond line can be clearly seen between the two diffusion-bonded blocks in spite of recrystallization, as indicated by the white arrows in Fig. 2. In fact, this diffusion bonding interface can be regarded as an interfacial grain boundary, and the interfacial grain boundaries often migrate and transform into the curved grain boundaries at higher temperatures because of grain growth [31, 35]. However, the interfacial grain boundary (bond line) is still straight after the high-temperature bonding process. This is because many carbide precipitates (such as chromium carbides) are formed on the bond line, as will be shown later. These carbide precipitates are relatively stable at higher bonding temperatures and are almost unaffected by the post-bond heat treatment. Consequently, the migration of interfacial bond line is suppressed during diffusion bonding and post-bond heat treatments due to the strong pinning effect of these carbide precipitates at the bond line. The detailed distribution and

Figure 2 EBSD microstructures of **a** the as-received Alloy 690 and **b** diffusion-bonded joint, and **c** SEM and **d** EBSD high-magnification microstructures of the diffusion-bonded joint.
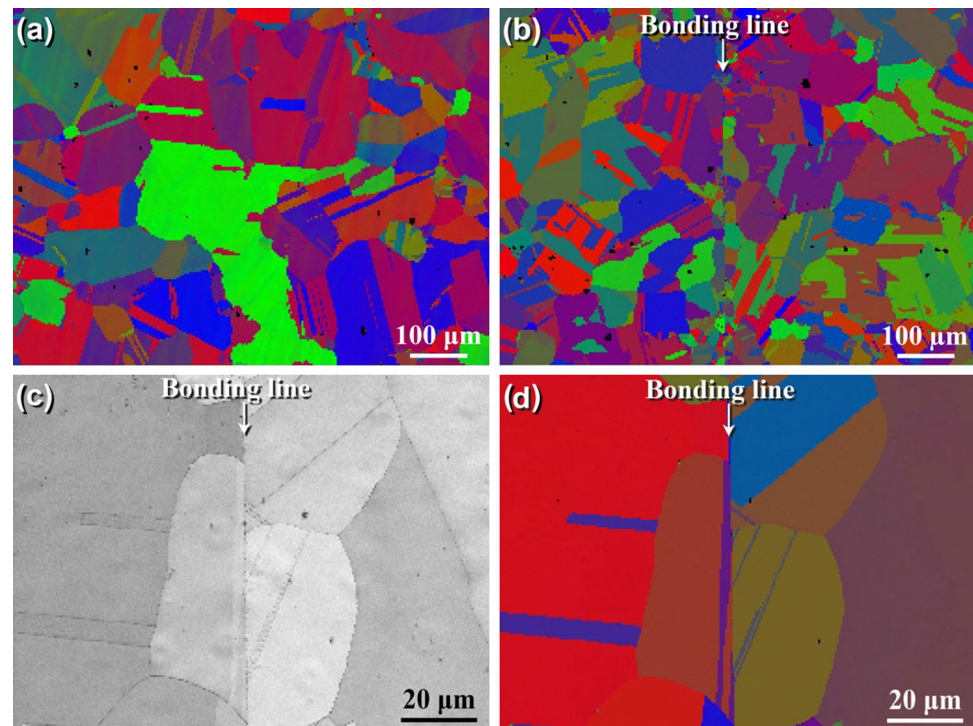
morphology of the interfacial carbide precipitates will be presented in the following section.

Effect of high-temperature exposure on the microstructure

Figure 3 shows the surface morphologies of the diffusion-bonded joints after S-CO₂ exposure at different temperatures. As shown in the figure, protective chromia scale is successfully developed on the joint surface for all the exposure conditions, which is coincident with the previous studies [11, 13, 14]. It should be noted that the bonding line was not discernable from the surface morphologies of oxide scales as there is no clear difference in corrosion behavior between the bonding line and the nearby regions [12]. It also can be seen that many chromia particles are formed on the oxide scale and the size of these particles increases with the increase in exposure temperature. Moreover, some scratches can be clearly observed on the oxide surface of the diffusion-bonded joint exposed at 550 °C (Fig. 3a). This is because the thickness of chromia scale formed at a lower temperature is too thin to cover the original polishing scratches.

Figures 4 and 5 show the cross-sectional microstructures and EDS elemental mapping results of the central bonding regions (about 0.25 mm depth

from the surface, half of the specimen thickness) of the joints with and without exposure in the S-CO₂ environment. This measure ensures that the obtained cross-sectional microstructures are only affected by the exposure temperature. It is noted that the authors reported the near-surface microstructure evolution of the diffusion-bonded Alloy 600 during S-CO2 exposure [12], but the microstructure evolution far from the surface was not analyzed. For the as-bonded joint, some white precipitates are distributed at the bonding line and grain boundaries (Fig. 4a). From the high-magnification image (Fig. 4a-1), it can be seen that these white precipitates are discontinuously arranged along the bonding line and their size is very small. These discontinuous precipitates along the bonding line in the diffusion-bonded joints of Ni-based alloys were also observed in the previous report [36]. The corresponding elemental mapping results indicate that these precipitates are rich in C, O and Al compared with the nearby matrix (Fig. 5a). Meanwhile, the Cr enrichment in these precipitates cannot be distinguished in the Cr mapping image due to the higher Cr content in the matrix and the small phase size. Additional EDS point results (not shown here) reveal that the C and Cr values of these white precipitates are significantly higher than those of the near matrix, and the Al and O values of these

Figure 3 Surface morphologies of the diffusion-bonded joints exposed at different temperatures: **a** 550 °C, **b** 600 °C and **c** 650 °C.
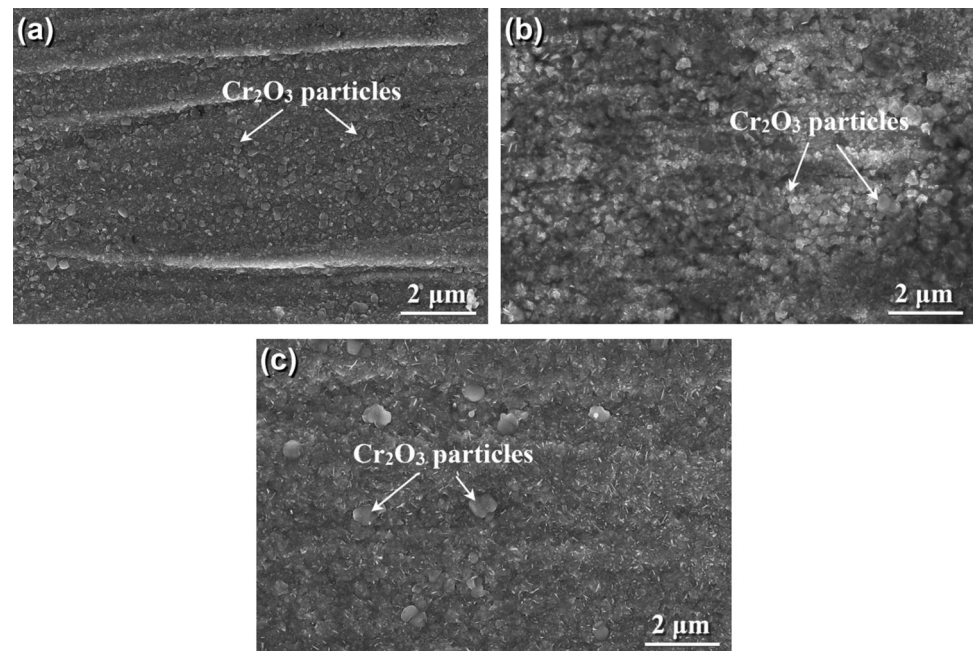

precipitates are slightly larger than the matrix. These results indicate that these white precipitates are possibly composed of Cr-rich carbides with a small amount of Al-rich oxides. This result is consistent with the description in previous studies [29, 31], in which the Cr- and/or Mo-rich carbides and Al-rich oxides were formed at the bonding line of Alloy 617 and Haynes 230 joints. These Cr-rich carbides and Al-rich oxides are relatively stable at high temperatures, which can serve as obstacles to prevent the grain growth across the bonding line and the migration of interfacial grain boundaries [37]. Therefore, the straight bonding line was retained in the joints after high-temperature bonding process, as shown in Fig. 2.

After exposure at 550 °C and 600 °C in the S-CO_2 environment, the discontinuous precipitates change to continuous strips and occupy all the grain boundaries and bonding line, as shown in Fig. 4b, c. With the increase in exposure temperature, the width of precipitate strips slightly increases, as shown in Fig. 4b-1 and c-1. The corresponding elemental mapping results reveal that more C and Cr are found at the bonding line, as shown in Fig. 5b, c. These results suggest more Cr-rich carbides are developed at the grain boundaries and bonding line after corrosion testing. Obviously, the reaction of C and Cr results in the formation of these Cr-rich carbides. It is well known that free C can be formed on the alloy

surface by the reaction of CO_2 with metallic elements or by the Boudouard reaction during the corrosion process [9, 10]. As a result, there is a doubt that whether the C comes from the nearby matrix (alloying C) or from the alloy surface. Recently, the present authors found that some C indeed penetrated through the oxide layer and resulted in the amorphous C layer at oxide/matrix interface in the diffusion-bonded Alloy 600 joints exposed to the S-CO_2 environment at 550 °C and 650 °C [12]. However, the carburized layer was very thin and the matrix far away from the surface was unaffected. Therefore, it can be inferred that the C needed to react with Cr to form the Cr-rich carbides in the bonding line region far away from the surface primarily comes from the nearby matrix. Meanwhile, due to mismatch in the atomic arrangement and the higher interfacial energy in the grain boundaries and bonding line, such regions would be the preferential nucleation sites for the precipitate [38]. Thus, Cr-rich carbides prefer to precipitate and grow at the grain boundaries and bonding line, and finally transform into the continuous strips during the long-term aging process. In addition, more alloying C and Cr can diffuse from the nearby matrix to the grain boundaries and bonding line at higher temperatures. Therefore, the width of the carbide strips increases when the exposure temperature increases from 550 to 600 °C.

Figure 4 Cross-sectional microstructures of the central bonding regions of the diffusion-bonded joints before and after corrosion test at different temperatures: **a** as-bonded joint, and after exposure to **b** 550 °C, **c** 600 °C and **d** 650 °C. The right images show the magnified microstructures of the corresponding left images marked by the red rectangles.
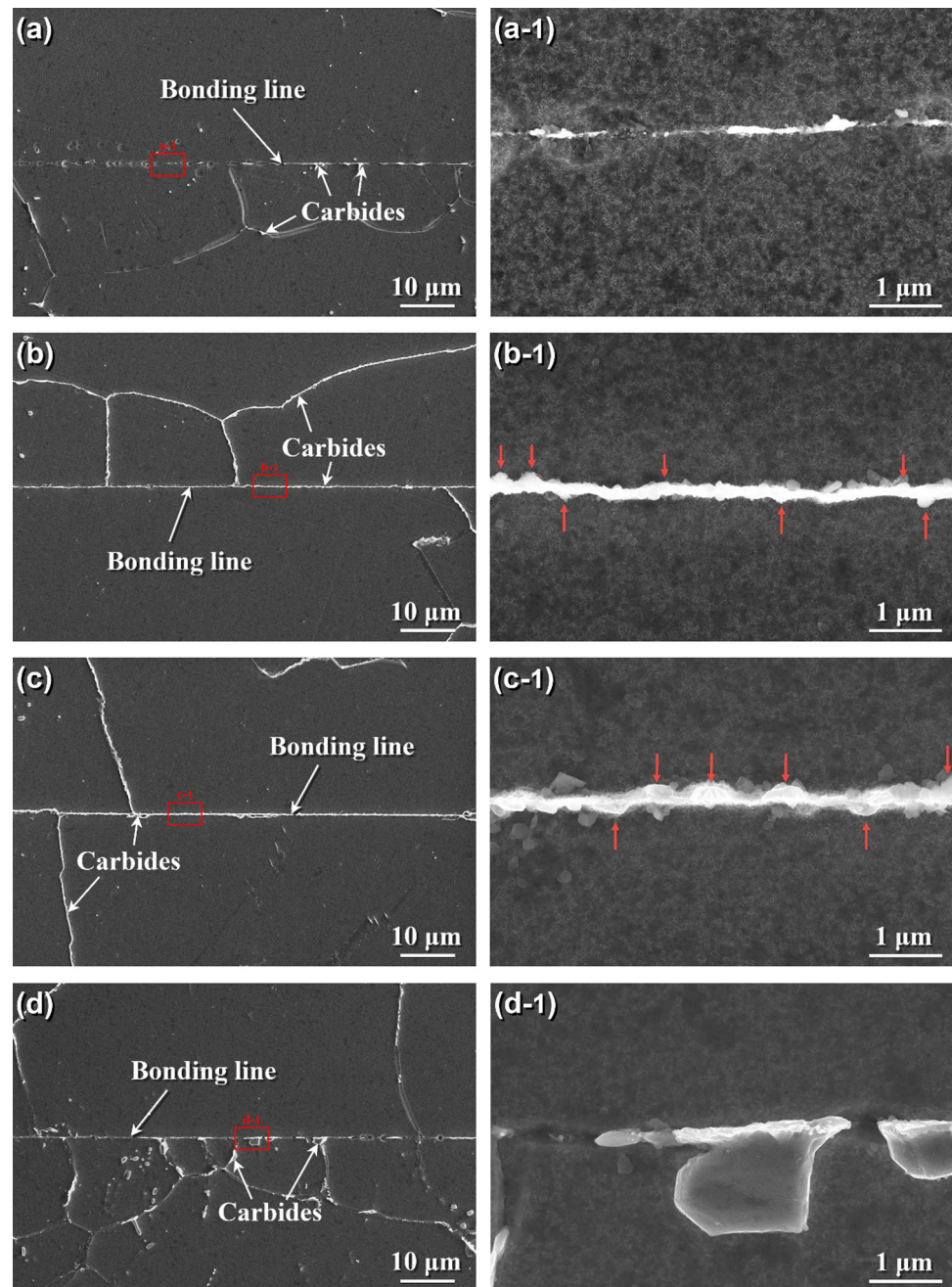
When the temperature further increases to 650 °C, the continuous carbides transform into discrete precipitates or particles, as shown in Fig. 4d. Many carbides are even larger than 1 μm (Figs. 4d-1, 5d). This indicates that the coarsening of Cr-rich carbides has been significantly accelerated at 650 °C for Alloy 690. This result is consistent with the bulk Alloy 690 in previous studies [39, 40]. Jiao et al. [39] found that the carbides grew obviously at 650 °C when the annealing time was only 20 h. Even at lower temperatures,

the coarsening of carbides on the grain boundaries was clearly observed in the long-term annealing process [40]. This growth of Cr-rich carbides may affect the mechanical properties of the diffusion-bonded joints, and this effect will be present in the next section.

Figure 5 SEM microstructures and corresponding elemental scanning maps of the bonding line region before and after corrosion test at different temperatures. **a** as-bonded joint, and after exposure to **b** 550 °C, **c** 600 °C and **d** 650 °C.
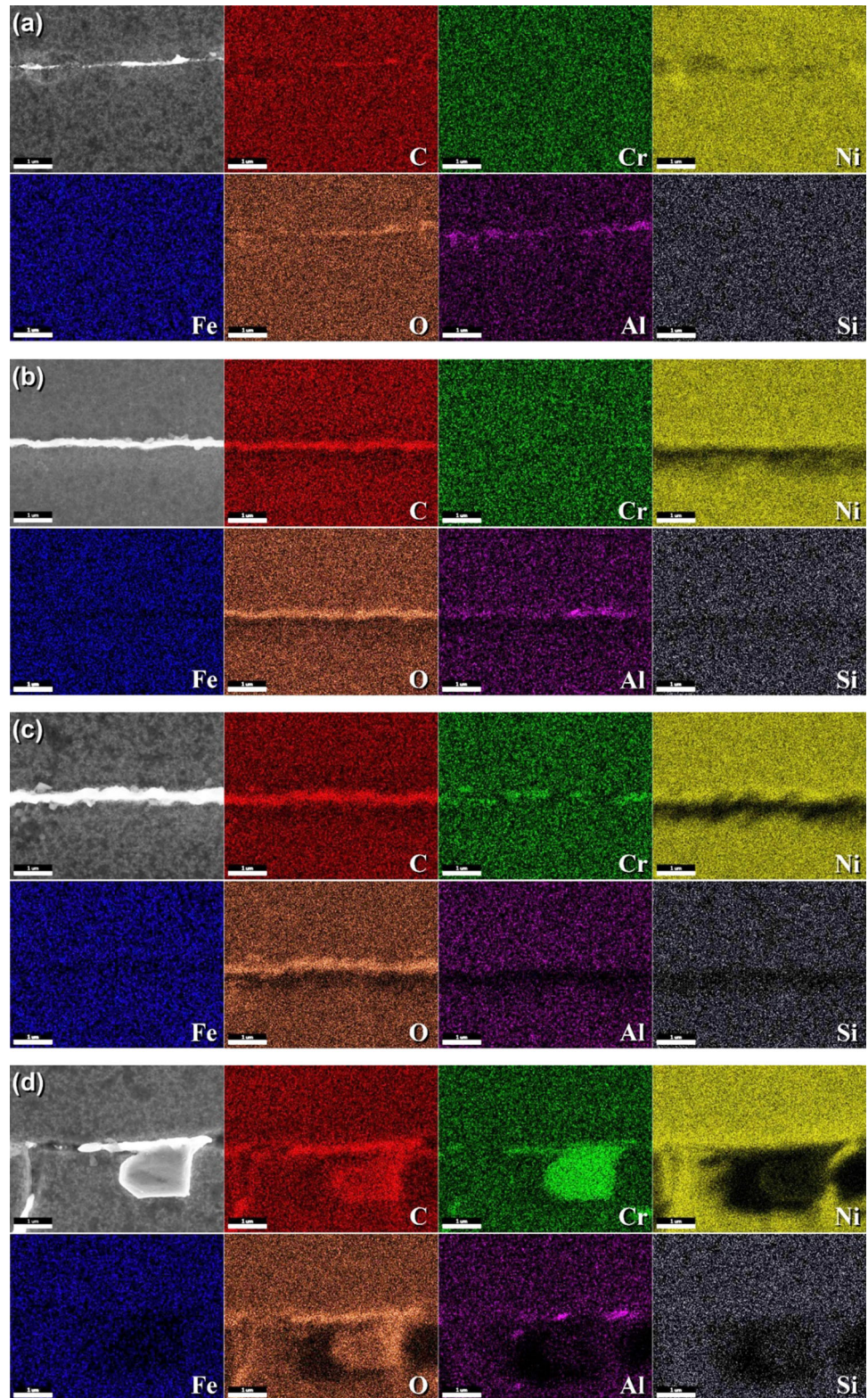
Effect of exposure temperature on the mechanical properties

Figure 6 shows the engineering stress–strain curves of the diffusion-bonded Alloy 690 joints with and without corrosion testing at different temperatures. It can be clearly seen that the necking occurs at the parent Alloy 690 for the joints before S-CO$_2$ exposure and after exposure at 550 °C and 600 °C, which suggests that the bonding strengths of these diffusion-bonded joints are higher than the parent materials. Meanwhile, the joint after exposure at 650 °C ruptures suddenly at the bonding line after a certain strain, which indicates that the bonding strengths of the diffusion-bonded joints degrade after exposure at a higher temperature.

Obviously, the degradation of bonding strengths is primarily caused by the growth of Cr-rich carbides at the grain boundaries and bonding line described in the previous section. In general, the steels and alloys with

fine carbides have superior mechanical properties, while the coarse carbides degrade the creep–fatigue and fracture resistances [41]. From this point of view, in the as-bonded condition, bonding strength would be good because there is only a small amount of fine carbides in the joint, as shown in Fig. 4a. Then, after exposure at 550 °C and 600 °C, the thin and continuous carbides are developed in the joints, as shown in Fig. 4b, c. However, these planar carbides would be less harmful to the mechanical properties. Firstly, most of the Cr-rich carbides in Ni-based alloys are M$_{23}$C$_6$-type carbides. The M$_{23}$C$_6$-type carbides have an FCC-like structure, and the planar M$_{23}$C$_6$-type carbides are usually coherent with the γ-matrix of FCC alloys with $\{111\}_\gamma//\{111\}_{M_{23}C_6}$, $\langle 111 \rangle_\gamma//\langle 111 \rangle_{M_{23}C_6}$ crystallographic relationships [41, 42]. This coherent structure provides a good combining effect between the grain matrixes and carbides. Moreover, the occurrence of grain boundary serration or carbide serration can further mitigate the coherent lattice distortion and result
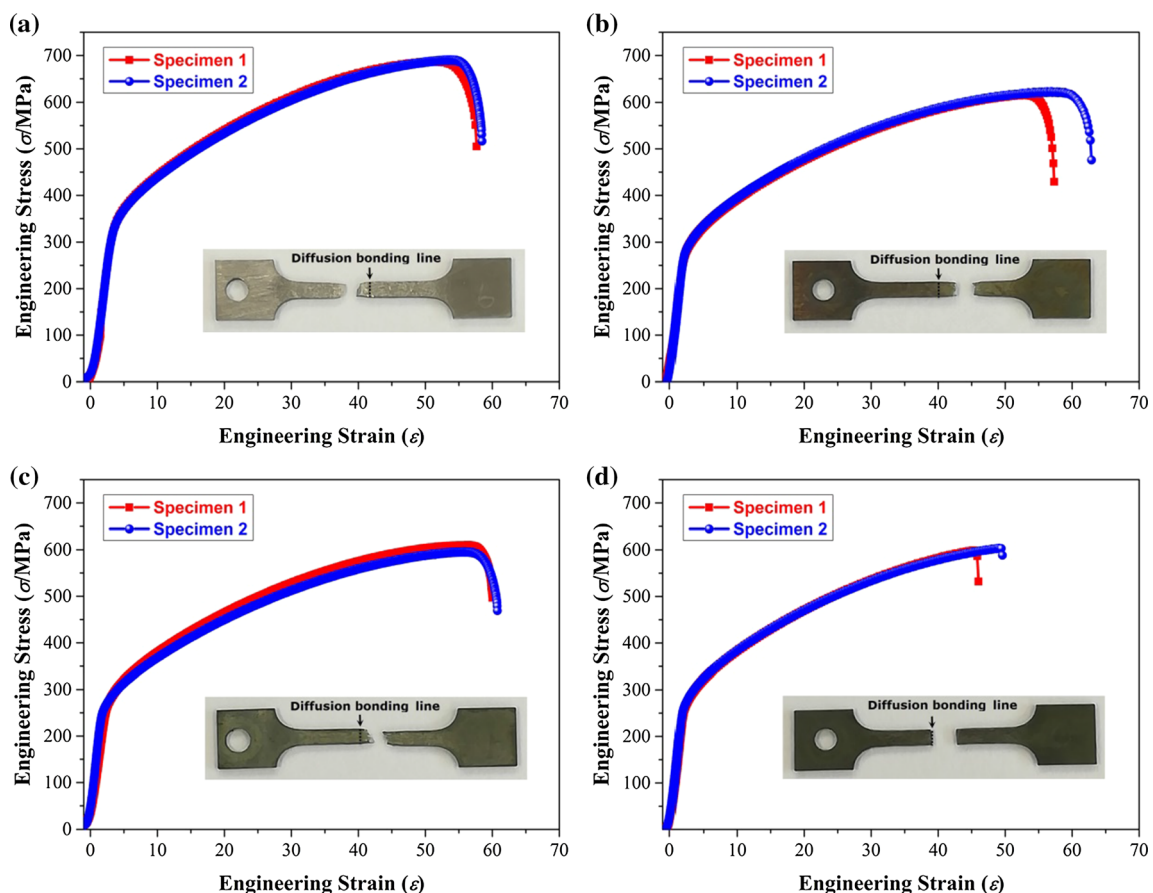

Figure 6 Engineering stress–strain curves of the diffusion-bonded joints before and after corrosion test at different temperatures: **a** as-bonded joint, and after exposure to **b** 550 °C, **c** 600 °C and **d** 650 °C. The insets are the corresponding photographs of the failed tensile specimens.

in a lower interfacial energy of matrixes and carbides [41, 43]. In the present study, the carbide serration is observed on the continuous carbides, as indicated by the red arrows in Fig. 4b-1, c-1. Therefore, these joints would have good tensile properties in spite of the continuous carbides occupying all the grain boundaries and bonding line. The occurrence of fracture at the parent Alloy 690 also indicates that the coherent bonding strength of the γ-matrixes with the continuous carbides at the bonding line is higher than that of the pure γ-matrixes in these joints. Otherwise, the fracture location will be the bonding line where the continuous carbides cross through the entire joints. Meanwhile, for the joint exposed at 650 °C, the discrete and coarse carbides are formed (Fig. 4d). These coarse carbides are difficult to maintain a coherent relationship with the matrix, and they may act as the nucleation sites for the microcracks during the tensile process [44]. Consequently, the bonding line becomes the weakest location of the diffusion-bonded joint exposed at 650 °C.

The ultimate tensile strength and elongation of the diffusion-bonded joints can be obtained from the stress–strain curves shown in Fig. 6. With the increase in exposure temperature, the ultimate tensile strength decreases; meanwhile, the elongation first slightly increases and then decreases at 650 °C. The decrease in tensile strength with exposure temperature is probably attributed to the excessive consumption of the alloying C and Cr contents in the grain matrixes during the long-term exposure testing. It is well known that increasing C content can increase the strength of steels and alloys and reduce the ductility [45]. Moreover, previous studies showed that the Cr content played an important role in the strengths of Ni-based alloys, i.e., the reduction in Cr concentration in the matrix was associated with the decrease in strength and the increase in elongation [42, 46]. After exposure to the high-temperature S-CO$_2$ environment, massive Cr-rich carbides are developed at the grain boundaries and bonding line of the diffusion-bonded joints, and the carbides increase obviously with the increase in exposure temperature. Meanwhile, the alloying C and Cr contents in the grain matrixes would decrease correspondingly with the increase in temperature. Hence, the tensile strength of the diffusion-bonded joints decreases and the elongation increases with increasing temperature. At 650 °C, the drop of elongation is mainly attributed to the break of the weak bonding

line, not related to the intrinsic properties of the grain matrixes of this joint.

For further validating this hypothesis, the Vickers microhardnesses of the grain matrix of these joints are examined and the results are shown in Fig. 7. It should be noted that all the indentations are located in the grains near the bonding line in order to only check the properties of the grain matrixes, as shown in the insets of Fig. 7. It can be seen that the microhardnesses of the grain matrix gradually decreases with the increase in exposure temperature. This tendency is similar to the ultimate tensile strength, indicating that the mechanical strengths of the grain matrixes are indeed degraded after exposure in the high-temperature S-CO$_2$ environment. In addition, the rebound of the indentations is more obvious for the exposed joints, as indicated by the red arrows in Fig. 7. This also suggests that the grain matrixes become soft after exposure in the S-CO$_2$ environment.

Although the tensile strength of the diffusion-bonded joints decreases and the elongation increases (except 650 °C) after exposure at high temperatures, the fracture toughness of diffusion-bonded Alloy 690 would not increase accordingly because of the brittleness of the continues carbides located at the bonding interface. Additional small punch tests confirm that the fracture toughness (small punch energy measured from the area below the load–displacement curve) of the diffusion-bonded Alloy 690 is reduced after aging at 600 °C for 1000 h compared with the as-received Alloy 690 and the diffusion-
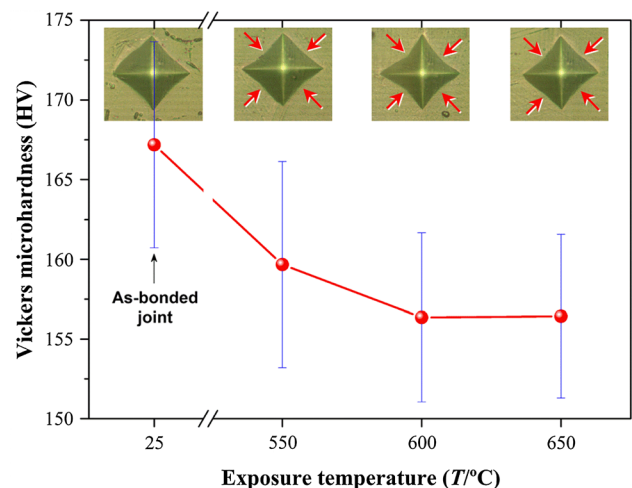

Figure 7 Vickers microhardness of the grain matrix as a function of exposure temperature. The insets are the morphologies of indentation.

bonded Alloy 690 without exposure, as shown in Fig. S1 in the supporting materials. This indicates that the long-term treatments at higher temperatures will lead to a reduced fracture toughness of the diffusion-bonded Alloy 690 associated with the carbide formation and growth at the bonding line.

## Fracture morphologies of the diffusion-bonded joints

To further investigate the mechanical response of the diffusion-bonded joints during the tensile test, the fracture morphologies of these joints after rupture are observed. Figure 8 shows the side-view fracture morphologies of the diffusion-bonded joints before and after S-CO_2 corrosion test at different temperatures. For the joints before and after exposure at 550 °C and 600 °C, the fracture surfaces are very irregular, which are consistent with the necking phenomena. However, the fracture surface is relatively straight for the joint exposed at 650 °C, further confirming that the fracture of this joint occurs at the bonding line. From the right magnified morphologies, it can be seen that many broken oxide scales adhere to the matrix. The wider separation distance of these broken oxide scales indicates that a large amount of deformation occurs in the matrixes, even for the joint exposed at 650 °C. In addition, there is no obvious crack in the matrixes in spite of the oxide scales damaged seriously. This indirectly verifies that the sub-scale matrix still possesses good mechanical properties after exposure in the high-temperature S-CO_2 environment. It is reasonable because the matrix affected by corrosion is very thin for the Ni-based alloys, as reported in our previous studies [10–12].

Figure 9 shows the top-view fracture morphologies of the joints before and after corrosion test at different temperatures. A ductile feature with many large dimples is present on the fracture surface of the as-bonded joint, as shown in Fig. 9a. The typical intergranular and cleavage features are not observed on the joint; rather, this joint breaks in a ductile fracture manner by the microvoid nucleation and coalescence [47]. The joints exposed at 550 °C and 600 °C also fracture in the ductile fracture manner because both the central and side fracture regions are occupied by the large dimples, as shown in Fig. 9b, c. Moreover,

some microcracks are detected on the fracture surfaces of these joints, and the number of microcracks increases with the increase in exposure temperature. The formation of microcracks is possibly attributed to the continuous carbides on the grain boundaries. In the process of large tensile deformation, the mismatch of strains between the carbides and the grains inevitably results in the higher plastic misfit stresses near the grain boundaries [48]. A large amount of microvoids can nucleate along the grain boundaries with higher stress concentration, and the growth and coalescence of these microvoids eventually lead to the formation of microcrack-like fracture surface. Other studies also observed that the increase in grain boundary carbides transformed the transgranular dimple fracture into a mixture mode of the transgranular and intergranular fracture, and the microcracks often occurred on the grain boundaries with more carbides in the Ni-based alloys [44, 49]. Although the intergranular fracture occurs at some surface regions of the two joints, the fracture mode is still a ductile fracture because many small dimples are presented on the microcrack-like fracture surfaces, as shown in Fig. 9b-1. This fracture mode ensures that the joints exposed at 550 °C and 600 °C have relatively high elongation.

The fracture morphology of the joint exposed at 650 °C is very different from the other joints, as shown in Fig. 9d. The entire fracture surface is almost flat without large dimple, indicating that the fracture of this joint occurs at the original bonding line and the fracture mode is near complete brittle fracture. There are many small craters embedded in the fracture surface, as indicated by red arrows in Fig. 9d-1, d-2. These craters were occupied by the larger carbides on the bonding line before tensile testing and are formed as a result of the carbides shedding after rupture. The high-magnification morphology of the central fracture regions clearly exhibits a large carbide and the associated crater, as shown in Fig. 10. The craters which originated from carbides were also observed in the diffusion-bonded Haynes 230 joint, which showed the brittle fracture [31]. In addition, many small dimples can be found from the high-magnification morphology (Fig. 10). This indicates that the nucleation and coalescence of microvoids occur at the bonding line in the first stage of the fracture process. However, further coalescence of

Figure 8 Side-view fracture morphologies of the diffusion-bonded joints before and after corrosion test at different temperatures: **a** as-bonded joint, and after exposure to **b** 550 °C, **c** 600 °C and **d** 650 °C. The right images show the magnified microstructures of the corresponding left images marked by the red rectangles.
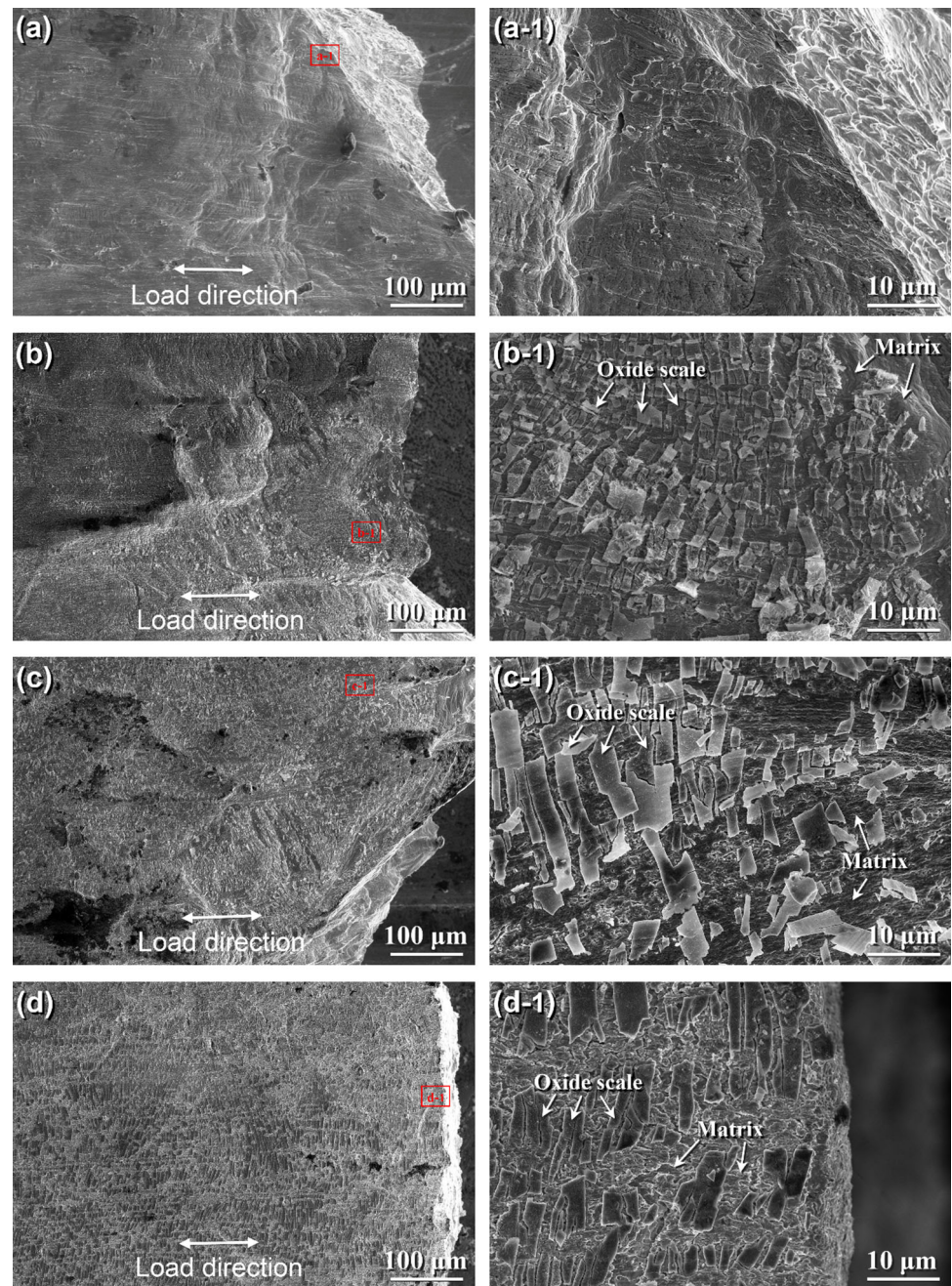
microvoids is restrained because of the higher stress concentration induced by the larger carbides, and the joint suddenly ruptures when the stresses exceed the interfacial bonding strength. This reason may induce the different tensile response and the brittle fracture for the diffusion-bonded joint after exposure at 650 °C.

Conclusions

Alloy 690 was joined by diffusion bonding, and the joints were exposed to the high-temperature S-CO$_2$ environment. The effect of S-CO$_2$ exposure on the microstructure and mechanical properties of the diffusion-bonded joints was evaluated. Based on the tensile tests and subsequent analysis, the following conclusions are drawn:
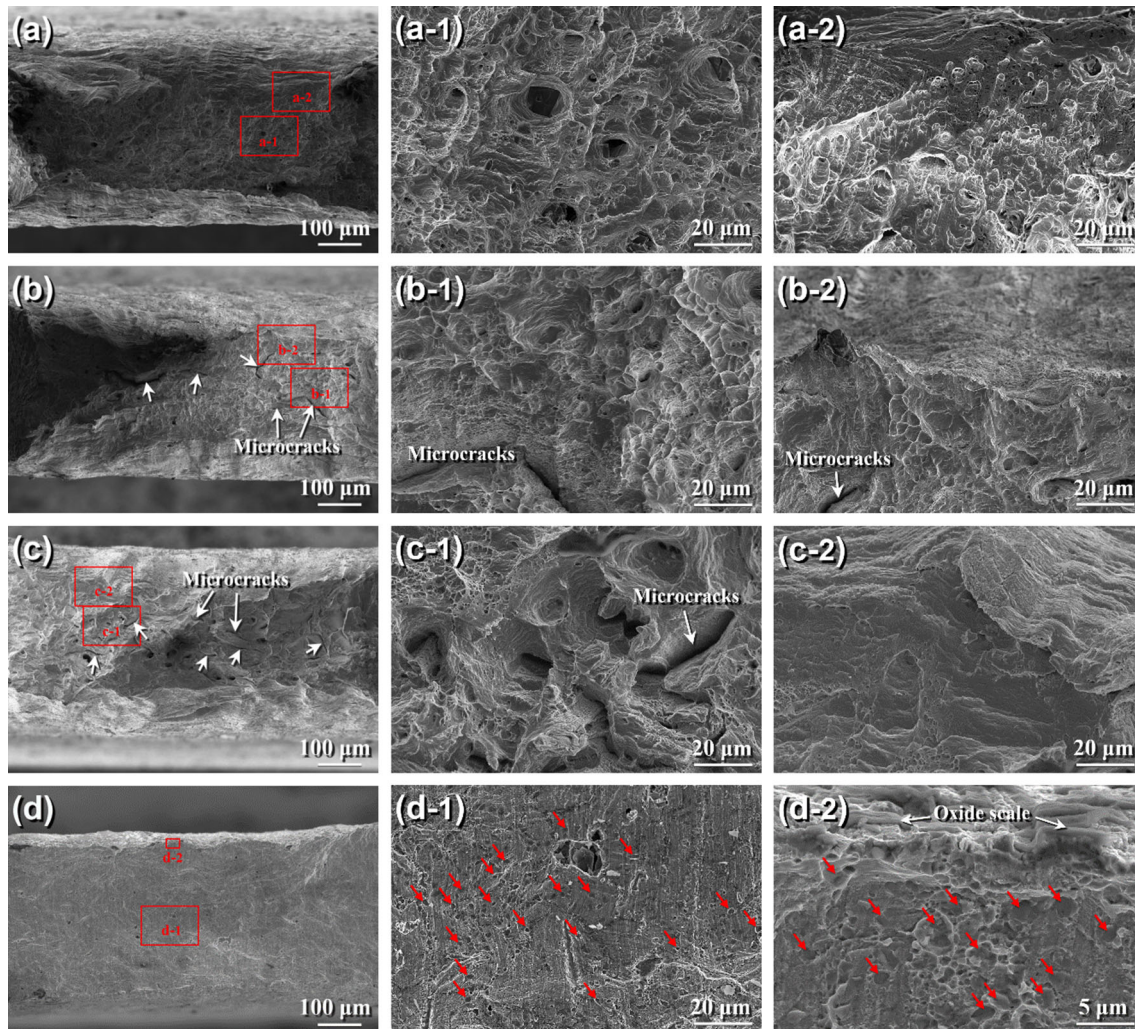
Figure 9 Top-view fracture morphologies of the diffusion-bonded joints before and after corrosion test at different temperatures: **a** as-bonded joint, and after exposure to **b** 550 °C, **c** 600 °C and **d** 650 °C. The central and right images show the magnified microstructures of the central and side fracture regions, as marked by the red rectangles in the corresponding left images.
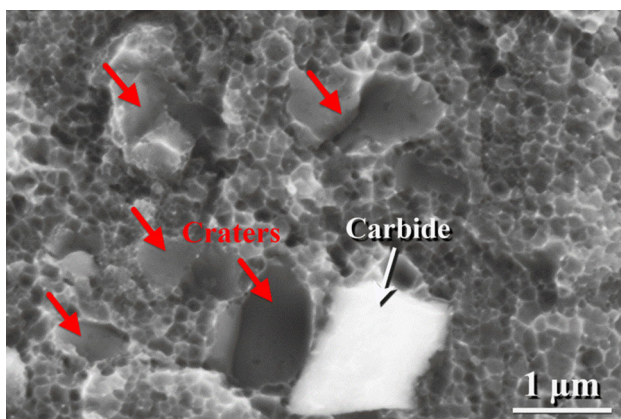

Figure 10 High-magnification morphology of the fracture regions of the diffusion-bonded joint exposed at 650 °C.

(1) In the as-bonded joint, some small carbides are discontinuously arranged along the bonding line. After exposure at 550 °C and 600 °C, the continuous carbides are developed in the joints and occupy all the grain boundaries and bonding line. The width of continuous carbides slightly increases with temperature. When the exposure temperature further increases to 650 °C, the continuous carbides change to the discrete large particles.

(2) With the increase in exposure temperature, the tensile strength decreases, while the elongation first slightly increases and then decreases at 650 °C. The decrease in mechanical strengths and the increase in elongation are probably attributed to the excessive consumption of the

alloying C and Cr contents in the grain matrixes. The degradation of bonding strengths and elongation of the joint exposed at 650 °C result from the growth of carbides.

(3) For the as-bonded joint and joints exposed at 550 °C and 600 °C, the fracture occurs at the parent Alloy 690, and the main fracture mode is the ductile dimple fracture. Some microcracks are presented in the exposed joints, and their formation is attributed to the continuous carbides on the grain boundaries. For the joint exposed at 650 °C, the fracture occurs at the bonding line with a manner of brittle fracture associated with the growth of carbides on bonding line.

Acknowledgements

Data availability

The raw/processed data required to reproduce these findings cannot be shared at this time due to technical or time limitations. They will be shared upon reasonable request.

Electronic supplementary material: The online version of this article (https://doi.org/10.1007/s108 53-019-04222-z) contains supplementary material, which is available to authorized users.

References

[1] Brun K, Friedman P, Dennis R (2017) Fundamentals and applications of supercritical carbon dioxide (sCO$_2$) based power cycles. Woodhead Publishing, Sawston

[2] Crespi F, Gavagnin G, Sánchez D, Martínez GS (2017) Supercritical carbon dioxide cycles for power generation: a review. Appl Energy 195:152–183

[3] Sharan P, Neises T, McTigue JD, Turchi C (2019) Cogeneration using multi-effect distillation and a solar-powered supercritical carbon dioxide Brayton cycle. Desalination 459:20–33

[4] Liang Z, Gui Y, Wang Y, Zhao Q (2019) Corrosion performance of heat-resisting steels and alloys in supercritical carbon dioxide at 650 °C and 15 MPa. Energy 175:345–352

[5] Kim ES, Oh CH, Sherman S (2008) Simplified optimum sizing and cost analysis for compact heat exchanger in VHTR. Nucl Eng Des 238:2635–2647

[6] Shah RK, Sekulic DP (2003) Fundamentals of Heat Exchanger Design. Wiley, Hoboken

[7] Lee Y, Lee JI (2014) Structural assessment of intermediate printed circuit heat exchanger for sodium-cooled fast reactor with supercritical CO$_2$ cycle. Ann Nucl Energy 73:84–95

[8] Sabharwall P, Clark DE, Mizia RE, Glazoff MV, McKellar MG (2013) Diffusion-welded microchannel heat exchanger for industrial processes. J Therm Serv Eng Appl 5:01109

[9] Subramanian GO, Lee HJ, Kim SH, Jang C (2018) Corrosion and carburization behaviour of Ni–xCr binary alloys in a high-temperature supercritical-carbon dioxide environment. Oxid Met 89:683–697

[10] Lee HJ, Kim H, Kim SH, Jang C (2015) Corrosion and carburization behavior of chromia-forming heat resistant alloys in a high-temperature supercritical-carbon dioxide environment. Corros Sci 99:227–239

[11] Lee HJ, Subramanian GO, Kim SH, Jang C (2016) Effect of pressure on the corrosion and carburization behavior of chromia-forming heat-resistant alloys in high-temperature carbon dioxide environments. Corros Sci 111:649–658

[12] Lee HJ, Kim SH, Jang C (2018) Characterization of Alloy 600 joints exposed to a high-temperature supercritical-carbon dioxide environment. Mater Charact 138:245–254

[13] Firouzdor V, Cao G, Sridharan K, Anderson M, Allen TR (2013) Corrosion of a stainless steel and nickel-based alloys in high temperature supercritical carbon dioxide environment. Corros Sci 69:281–291

[14] Holcomb GR, Carney C, Doğan ÖN (2016) Oxidation of alloys for energy applications in supercritical CO$_2$ and H$_2$O. Corros Sci 109:22–35

[15] Olivares RI, Young DJ, Marvig P, Stein W (2015) Alloys SS316 and Hastelloy-C276 in supercritical CO$_2$ at high temperature. Oxid Met 84:585–606

[16] Rouillard F, Furukawa T (2016) Corrosion of 9–12Cr ferritic–martensitic steels in high-temperature CO$_2$. Corros Sci 105:120–132

[17] Cao G, Firouzdor V, Sridharan K, Anderson M, Allen TR (2012) Corrosion of austenitic alloys in high temperature supercritical carbon dioxide. Corros Sci 60:246–255

[18] Tan L, Anderson M, Taylor D, Allen TR (2011) Corrosion of austenitic and ferritic-martensitic steels exposed to supercritical carbon dioxide. Corros Sci 53:3273–3280

[19] Zhu Z, Cheng Y, Xiao B, Khan HI, Xu H, Zhang N (2019) Corrosion behavior of ferritic and ferritic-martensitic steels in supercritical carbon dioxide. Energy 175:1075–1084

[20] Chen H, Kim SH, Kim C, Chen J, Jang C (2019) Corrosion behaviors of four stainless steels with similar chromium content in supercritical carbon dioxide environment at 650 °C. Corros Sci 156:16–31

[21] Chen H, Kim SH, Long C, Kim C, Jang C (2018) Oxidation behavior of high-strength FeCrAl alloys in a high-temperature supercritical carbon dioxide environment. Prog Nat Sci Mater Int 28:731–739

[22] Lee HJ, Kim SH, Kim H, Jang C (2016) Corrosion and carburization behavior of Al-rich surface layer on Ni-base alloy in supercritical-carbon dioxide environment. Appl Surf Sci 388:483–490

[23] Sah I, Kim D, Lee HJ, Jang C (2013) Development and oxidation resistance evaluation of Al-rich surface layer on Alloy 617. Surf Coat Technol 236:400–404

[24] Kim SH, Subramanian GO, Kim C, Jang C, Park KM (2018) Surface modification of austenitic stainless steel for corrosion resistance in high temperature supercritical-carbon dioxide environment. Surf Coat Technol 349:415–425

[25] Takeda T, Kunitomi K, Rorie T, Iwata K (1997) Feasibility study on the applicability of a diffusion-welded compact intermediate heat exchanger to next-generation high temperature gas-cooled reactor. Nucl Eng Des 168:11–21

[26] Hesselgreaves JE (2001) Compact heat exchangers: selection, design and operation. Pergamon Press, Oxford

[27] Mizia RE (2010) Scoping investigation of diffusion bonding for NGNP process application heat exchangers. Idaho National Laboratory Report, INL/PLN-3565

[28] Basuki W, Kraft O, Aktaa J (2012) Optimization of solid-state diffusion bonding of Hastelloy C-22 for micro heat exchanger applications by coupling of experiments and simulations. Mater Sci Eng A 538:340–348

[29] Mylavarapu SK, Sun X, Christensen RN, Unocic RR, Glosup RE, Patterson MW (2012) Fabrication and design aspects of high-temperature compact diffusion bonded heat exchangers. Nucl Eng Des 249:49–56

[30] Kapoor M, Dogan O, Rozman K, Hawk J, Wilson A, Estrange T, Narayanan V (2016) Diffusion bonding of H230 Ni-superalloy for application in microchannel heat exchangers. In: The 5th international symposium-

supercritical CO_2 power cycles, San Antonio, Texas, 28–31 March 2016

[31] Sah I, Kim D, Lee HJ, Jang C (2013) The recovery of tensile ductility in diffusion-bonded Ni-base alloys by post-bond heat treatments. Mater Des 47:581–589

[32] Dostal V, Hejzlar P, Driscoll MJ (2006) High-performance supercritical carbon dioxide cycle for next-generation nuclear reactors. Nucl Technol 154:265–282

[33] Sakai T, Belyakov A, Kaibyshev R, Miura H, Jonas JJ (2014) Dynamic and post-dynamic recrystallization under hot, cold and severe plastic deformation conditions. Prog Mater Sci 60:130–207

[34] Nah JJ, Kang HG, Huha MY, Engler O (2008) Effect of strain states during cold rolling on the recrystallized grain size in an aluminum alloy. Scr Mater 58:500–503

[35] Zhang JY, Sun MY, Xu B, Li DZ (2018) Interfacial microstructural evolution and metallurgical bonding mechanisms for IN718 superalloy joint produced by hot compressive bonding. Metall Mater Trans B 49:2152–2162

[36] Shirzadi AA, Wallach ER (2004) New method to diffusion bond superalloys. Sci Technol Weld Join 9:37–40

[37] Gladman T (1966) On the theory of the effect of precipitate particles on grain growth in metals. Proc R Soc Lond A 294:298–309

[38] Gottstein G (2004) Physical foundations of materials science. Springer, Berlin

[39] Jiao SY, Zhang MC, Zheng L, Dong JX (2010) Investigation of carbide precipitation process and chromium depletion during thermal treatment of Alloy 690. Metall Mater Trans A 41:26–42

[40] Kai JJ, Yu GP, Tsai CH, Liu MN, Yao SC (1989) The effects of heat treatment on the chromium depletion, precipitate evolution, and corrosion resistance of INCONEL alloy 690. Metall Trans A 20:2057–2067

[41] Lo KH, Shek CH, Lai JKL (2009) Recent developments in stainless steels. Mater Sci Eng R 65:39–104

[42] Hua R, Bai G, Li J, Zhang J, Zhang T, Fu H (2012) Precipitation behavior of grain boundary $M_{23}C_6$ and its effect on tensile properties of Ni–Cr–W based superalloy. Mater Sci Eng A 548:83–88

[43] Hong HU, Nam SW (2002) The occurrence of grain boundary serration and its effect on the $M_{23}C_6$ carbide characteristics in an AISI 316 stainless steel. Mater Sci Eng A 332:255–261

[44] Sundararaman M, Mukhopadhyay P, Banerjee S (1997) Carbide precipitation in nickel base superalloys 718 and 625 and their effect on mechanical properties. Superalloys 718:625–706

[45] Wei CN, Bor HY, Chang L (2010) The effects of carbon content on the microstructure and elevated temperature

tensile strength of a nickel-base superalloy. Mater Sci Eng A 527:3741–3747

[46] Jena AK, Chaturvedi MC (1984) The role of alloying elements in the design of nickel-base superalloys. J Mater Sci 19:3121–3139. https://doi.org/10.1007/BF00549796

[47] Van Stone RH, Cox TB, Low JR, Psioda JA (1985) Microstructural aspects of fracture by dimpled rupture. Int Metals Rev 30:157–180

[48] Ott RT, Sansoz F, Molinari JF, Almer J, Ramesh KT, Hufnagel TC (2005) Micromechanics of deformation of metallic-glass–matrix composites from in situ synchrotron strain measurements and finite element modeling. Acta Mater 53:1883–1893

[49] Kim D, Sah I, Jang C (2011) Effects of aging in high temperature helium environments on room temperature tensile properties of nickel-base superalloys. Mater Sci Eng A 528:1713–1720

Springer